Solar Phys
DOI 10.1007/s11207-015-0662-7

Simulations of Gyrosynchrotron Microwave Emission from an Oscillating 3D Magnetic Loop

A.A. Kuznetsov[1] · T. Van Doorsselaere[2] · V.E. Reznikova[2,3]

Received: 21 November 2014 / Accepted: 24 February 2015

Abstract Radio observations of solar flares often reveal various periodic or quasi-periodic oscillations. Most likely, these oscillations are caused by magnetohydrodynamic (MHD) oscillations of flaring loops which modulate the emission. Interpreting the observations requires comparing them with simulations. We simulated the gyrosynchrotron radio emission from a semicircular (toroidal-shaped) magnetic loop containing sausage-mode MHD oscillations. The aim was to detect the observable signatures specific to the considered MHD mode and to study their dependence on the various source parameters. The MHD waves were simulated using a linear three-dimensional model of a magnetized plasma cylinder; both standing and propagating waves were considered. The curved loop was formed by replicating the MHD solutions along the plasma cylinder and bending the cylinder; this model allowed us to study the effect of varying the viewing angle along the loop. The radio emission was simulated using a three-dimensional model, and its spatial and temporal variations were analyzed. We considered several loop orientations and different parameters of the magnetic field, plasma, and energetic electrons in the loop. In the model with low plasma density, the intensity oscillations at all frequencies are synchronous (with the exception of a narrow spectral region below the spectral peak). In the model with high plasma density, the emission at low frequencies (where the Razin effect is important) oscillates in anti-phase with the emissions at higher frequencies. The oscillations at high and low frequencies are more pronounced in different parts of the loop (depending on the loop orientation). The layers where the line-of-sight component of the magnetic field changes sign can produce additional peculiarities in the oscillation patterns.

Keywords Coronal seismology · Flares, waves · Oscillations, solar · Radio bursts, microwave · Waves, magnetohydrodynamic

✉ A.A. Kuznetsov
a_kuzn@iszf.irk.ru

T. Van Doorsselaere
tom.vandoorsselaere@wis.kuleuven.be

1 Institute of Solar-Terrestrial Physics, Irkutsk 664033, Russia

2 CmPA, Department of Mathematics, KU Leuven, 3001 Leuven, Belgium

3 Radiophysical Research Institute (NIRFI), Nizhny Novgorod 603950, Russia

Published online: 10 March 2015

1. Introduction

Waves and oscillations are common phenomena in solar flares. They are believed to reveal themselves as quasi-periodic pulsations in spatially unresolved observations at different wavelengths (see, *e.g.*, the review of Nakariakov and Melnikov, 2009) and have been directly detected using the EUV observations with high spatial resolution (Nakariakov *et al.*, 1999; Aschwanden *et al.*, 1999; De Moortel and Nakariakov, 2012). In particular, the observed periodicities of the quasi-periodic pulsations in the radio emission, hard X-rays, and γ-rays (from a fraction of a second to several minutes) agree with the expected magnetohydrodynamic (MHD) timescales, which strongly suggests a close relationship between the pulsations and the MHD waves and oscillations (Nakariakov and Melnikov, 2009; De Moortel and Nakariakov, 2012). It should be noted, however, that the solar quasi-periodic pulsations are usually superimposed on a rapidly varying background, so that recovering their parameters is difficult; some previously reported conclusions may be unreliable because of the methodology used (Gruber *et al.*, 2011).

Observations of the waves and oscillations in the flares can be used to diagnose the quasi-periodic magnetic reconnection processes that are believed to be the most probable source of these oscillations (*e.g.*, Kliem, Karlický, and Benz, 2000). The MHD waves and oscillations can also be used to diagnose the coronal plasma and magnetic field parameters ("coronal seismology"; see, *e.g.*, Nakariakov and Verwichte, 2005). Moreover, the waves and oscillations are believed to play a key role in the energy transfer both in the quiet corona (*e.g.*, Erdélyi, 2006) and in the flares (Fletcher and Hudson, 2008); they can modulate and/or trigger the magnetic reconnection processes (Chen and Priest, 2006; Doyle, Popescu, and Taroyan, 2006; Nakariakov *et al.*, 2006) and thus greatly affect the behavior of unstable active regions and development of the solar flares.

One of the potential observable manifestations of MHD waves is quasi-periodic pulsation of radio emission (*e.g.*, Aschwanden, 1987; Nakariakov and Melnikov, 2009; Kupriyanova *et al.*, 2010), because these waves can modulate both the coherent and incoherent radio emission mechanisms. Interpreting the observed quasi-periodic pulsations requires comparing the observations with simulations to determine the origin of the pulsations (because they can be caused not only by the MHD waves but also, *e.g.*, by quasi-periodic injection of energetic particles); if the oscillations are due to waves, it allows us to identify the wave mode and other characteristics of the MHD waves. In turn, identifying the wave mode is of high importance for the development of the coronal seismology. As a rule, the basic characteristics of the pulsations (such as the period) have no unique interpretation and therefore some more subtle features (such as the relations between the pulsations observed in different spectral channels) have to be analyzed (Fleishman, Bastian, and Gary, 2008; Mossessian and Fleishman, 2012).

Perhaps the best tool for studying the physical parameters and processes in solar flares is their microwave emission, because it is produced mainly by the incoherent gyrosynchrotron radiation mechanism, which is (a) relatively simple and well studied (Melrose, 1968; Ramaty, 1969) and (b) highly sensitive to the magnetic field and plasma parameters. Many articles have been dedicated to simulating the gyrosynchrotron emission in solar flares. In particular, two-dimensional (2D) models (*e.g.*, Alissandrakis and Preka-Papadema, 1984; Klein and Trottet, 1984; Preka-Papadema and Alissandrakis, 1988; Kucera *et al.*, 1993; Kundu *et al.*, 2001) and three-dimensional (3D) models (*e.g.*, Preka-Papadema and Alissandrakis, 1992; Bastian, Benz, and Gary, 1998; Nindos *et al.*, 2000; Simões and Costa, 2006; Costa *et al.*, 2013) have been employed to account for the structure of the emitting region. Some simulations involve the magnetic field structure obtained by extrapolating the

observed photospheric magnetograms (*e.g.*, Gary, Fleishman, and Nita, 2013; Kuznetsov and Kontar, 2015), take into account anisotropy of the emitting electrons (*e.g.*, Fleishman and Melnikov, 2003; Altyntsev *et al.*, 2008; Simões and Costa, 2010; Kuznetsov, Nita, and Fleishman, 2011) and/or evolution of the electron distributions during flares (*e.g.*, Tzatzakis, Nindos, and Alissandrakis, 2008; Reznikova *et al.*, 2009; Kuznetsov and Zharkova, 2010; Kuznetsov and Melnikov, 2012). However, possible modulation of the emission by MHD waves has been studied only in a few works and by using relatively simple models (Kopylova, Stepanov, and Tsap, 2002; Nakariakov and Melnikov, 2006; Reznikova *et al.*, 2007; Mossessian and Fleishman, 2012). Recently, Reznikova, Antolin, and Van Doorsselaere (2014) have simulated the gyrosynchrotron radio emission from an oscillating magnetic cylinder (with standing sausage waves). It was found that even for the simple model considered (a straight cylinder), calculating the emission requires 3D simulations that also take into account the spatial structure of the MHD waves because the results can differ from simple estimates for a spatially homogeneous source (*cf.* Reznikova *et al.*, 2007; Mossessian and Fleishman, 2012). At the same time, another complication arises from the fact that the solar flaring loops are evidently curved (in contrast to the model of Reznikova, Antolin, and Van Doorsselaere (2014)). This work is dedicated to simulating the radio emission from such curved loops.

Simulation of MHD waves in flaring loops is a nontrivial task. Oscillation modes of a straight overdense cylinder of infinite length are well studied (Edwin and Roberts, 1983; Nakariakov and Verwichte, 2005, *etc.*), and the numerical simulations can be greatly simplified by using the analytical results. However, these results are not applicable to curved loops (Van Doorsselaere *et al.*, 2004). Variation of the plasma and magnetic field parameters as well as of the loop radius with height presents even more difficulties (Andries *et al.*, 2005; Andries and Cally, 2011). Therefore in this work we use a simplified model in which an oscillating cylinder is artificially bent to form a semi-circular loop without actually using the wave relations in a semi-torus; the magnetic field, plasma density and temperature, and the loop radius (in the equilibrium state, *i.e.*, without oscillations) are assumed to be constant along the loop. The main aim of this model is to study the effect of varying the viewing angle (*i.e.*, the angle between the local magnetic field and the line of sight) along the loop. Although such a model cannot correctly describe the entire loop, it can reproduce the effects of the MHD oscillations in local parts of the loop, where the effects of the loop curvature and inhomogeneity on the MHD wave parameters are negligible. We consider the incoherent gyrosynchrotron radiation of energetic electrons that contributes most to the flare emission in the microwave range.

The simulation model is described in Section 2. The simulation results are presented and discussed in Section 3. The conclusions are drawn in Section 4.

2. Model

2.1. MHD Waves

We used the model described earlier by Zaitsev and Stepanov (1975), Edwin and Roberts (1983), Antolin and Van Doorsselaere (2013), *etc.* In this model the magnetic field is directed along the axis of an overdense cylinder. The plasma density and temperature inside the cylinder are higher than outside, while the magnetic field strength inside the cylinder is lower than outside to maintain the pressure balance. We consider the azimuthally symmetric case when all parameters depend only on the distance along the cylinder axis z and the

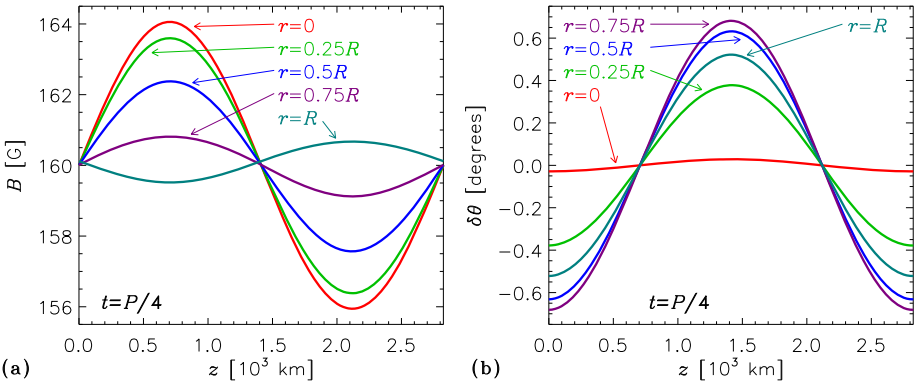

Figure 1 Profiles of the magnetic field strength (a) and direction relative to the tube axis (b) in the oscillating magnetic tube at different distances from the tube axis. The standing wave, low-density model (see Table 1) is considered; one wavelength is shown. Profiles of the plasma density and temperature are similar to those of the magnetic field.

distance from this axis r. In an equilibrium case, the magnetic field, plasma density, and temperature are assumed to be constant inside and outside the cylinder; they experience a sharp jump at the cylinder boundary (at $r = R$).

The formulae describing the MHD disturbances are given, *e.g.*, in the works of Zaitsev and Stepanov (1975), Edwin and Roberts (1983), Antolin and Van Doorsselaere (2013), and Reznikova, Antolin, and Van Doorsselaere (2014); see especially the article of Reznikova, Antolin, and Van Doorsselaere (2014), where the solutions of those equations are presented for the same conditions as used in this work. Therefore we describe the properties of the MHD waves only briefly. We consider the sausage mode – the compressible azimuthally symmetric ($m = 0$) oscillations that affect both the magnetic field and plasma density and temperature. We consider both the standing and propagating waves, which are described by the relations

$$A_{\rm stand} \propto \sin(\omega t)\sin(kz + \varphi_A), \qquad A_{\rm prop} \propto \sin(\omega t - kz + \varphi_A), \tag{1}$$

where A is the wave amplitude (*e.g.*, in velocity), ω and k are the wave frequency and wavenumber, and φ_A is the initial phase.

Figure 1 presents an example of how the parameters vary with the coordinates in a standing wave (the oscillation phase is chosen to provide the strongest deviation from equilibrium). In general, the axial magnetic field B_z, plasma density n_0, and temperature T_0 vary in phase, and their variations are strongest at the cylinder axis (we are interested only in the parameters inside the cylinder, because, as shown below, this is the region where the radio emission is assumed to be generated). Variations of these parameters decrease with increasing r and become zero at some radial distance r_* nearby the cylinder boundary ($r_* \simeq 0.9R$ for the parameters considered here). Then the amplitude of the variations increases slightly, but they are now in anti-phase with the variations of the same parameters in the inner part of the cylinder. Variations of the radial magnetic field B_r are shifted by 1/4 period with respect to other parameters; they are zero at the cylinder axis and reach their maximum at $r = r_*$ (without the phase reversal at that radial distance). Since we consider low-amplitude oscillations, we have $|B_r| \ll |B_z|$ (we recall that B_z includes here both the equilibrium magnetic field B_0 and the perturbed field component δB_z, *i.e.*, $B_z = B_0 + \delta B_z$). The radial component

Table 1 Parameters of the MHD models: a) cylinder radius (R), magnetic fields (B), plasma densities (n_0), and temperatures (T_0) inside (in) and outside (out) the cylinder in the equilibrium state, concentration of the energetic electrons (n_b) inside the cylinder in the equilibrium state; b) wavelength (λ) and period (P) of the sausage mode, strongest deviations of the magnetic field strength (δB), magnetic field direction ($\delta\theta$), plasma density (δn_0), plasma temperature (δT_0), and concentration of the energetic electrons (δn_b) inside the cylinder from the respective equilibrium values.

Model	Low-density	High-density
Equilibrium cylinder parameters		
R [km]	1000	1000
$B_{\rm in}$ [G]	160	50
$B_{\rm out}$ [G]	161	56
$n_{0\ \rm in}$ [cm^{-3}]	4×10^9	10^{10}
$n_{0\ \rm out}$ [cm^{-3}]	10^9	3×10^9
$T_{0\ \rm in}$ [K]	10^7	10^7
$T_{0\ \rm out}$ [K]	2×10^6	2×10^6
$n_{\rm b\ in}$ [cm^{-3}]	10^8	2.5×10^8
Wave parameters		
λ [km]	2825	2825
P [s]	0.35	1.5
$(\delta B_{\rm in})_{\rm max}$ [G]	4.05	2.78
$(\delta\theta_{\rm in})_{\rm max}$	0.69°	1.52°
$(\delta n_{0\ \rm in})_{\rm max}$ [cm^{-3}]	1.0×10^8	6.0×10^8
$(\delta T_{0\ \rm in})_{\rm max}$ [K]	1.7×10^5	4.1×10^5
$(\delta n_{\rm b\ in})_{\rm max}$ [cm^{-3}]	2.5×10^6	1.5×10^7

$B_r = \delta B_r$ makes almost no contribution to the resulting magnetic field strength; however, it mildly affects the magnetic field direction and causes it to deviate from the cylinder axis. Variations of the cylinder radius due to the MHD oscillations are very small and do not affect the radio emission.

The propagating sausage wave looks like the structure shown in Figure 1 moving along the z axis. All other properties of this wave (including the phase relations between different parameters) are the same as for the standing wave.

We consider two sets of model parameters, the same as have been used in the work of Reznikova, Antolin, and Van Doorsselaere (2014); the parameters are listed in Table 1. The parameters were chosen to provide the same wavelength λ for the given cylinder radius R. In the calculations below, we mainly use the low-density model because those conditions are more favorable for generating the gyrosynchrotron radio emission. In the high-density model, the emission intensity is usually lower; at low frequencies, the emission becomes strongly affected by the Razin effect (see Section 3.4.3).

2.2. Source Geometry

As stated before, the aim of this work is to study the effect of the loop curvature on the radio emission. For this, we have created a model of semi-circular (semi-toroidal) loops by bending the above-mentioned overdense cylinder (see Figure 2). In this case, the longitudinal coordinate within the cylinder z is transformed into the distance along the loop axis and the radial coordinate r – into the distance from the loop axis (the explicit formulae are given in the Appendix); this allows us to obtain the plasma and magnetic field parameters at any given point. Since the lengths of the solar flaring loops are usually much greater than their radii, we created the models by stacking several MHD simulation blocks (each corresponding to one wavelength, like in Figure 1) along the loop. As the "basic" model, we used the

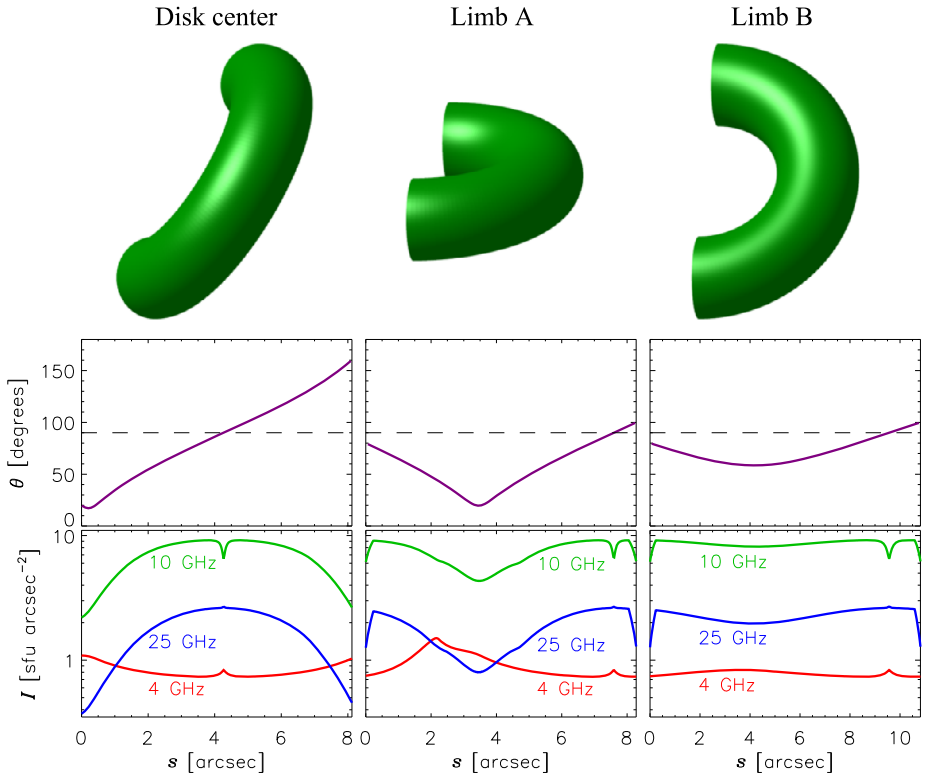

Figure 2 Three orientations of the model magnetic loop: 3D views of the loop (top row); profiles of the viewing angle (relative to the magnetic field, in the equilibrium state) along the loop axis (middle row); simulated profiles of the radio intensity in the equilibrium state at different frequencies (for the low-density model and the electron spectral index of $\delta = 4$) along the loop axis (bottom row). The visible coordinate along the loop s is measured from the upper footpoint (as shown in the 3D views).

loop containing three wavelengths; this loop has a length of 8475 km and a height (*i.e.*, the curvature radius) of about 2700 km.

The loop orientation is described in general by three Euler angles. However, since rotation around the line of sight does not provide any new information (it results simply in the same rotation of the simulated radio images), it is sufficient to consider the variation of only two angles (Kuznetsov, Nita, and Fleishman, 2011). We assumed that the loop is vertical and located at the solar equator. The loop orientation is described by two angles: the angle ψ between the loop plane and the equatorial plane, and the longitude λ. A possible loop inclination is not considered for the same reason as described above: for a vertical loop, the variation of the angles ψ and λ is sufficient to obtain any possible loop orientation with respect to the observer (with an accuracy up to the rotation around the line of sight); therefore our results are applicable to inclined loops as well. However, we note that the loop locations at the solar disk, which are discussed below, should be treated as approximate (illustrative) because they only correspond to the zero inclination.

We cannot present the results for all possible orientations here; therefore we focus on three illustrative cases (see Figure 2 and Table 2):

Table 2 Orientations of the magnetic loop used in the simulations: the angle relative to the equatorial plane (ψ) and the longitude (λ).

Orientation	Disk center	Limb A	Limb B
ψ	60°	20°	60°
λ	20°	80°	80°

a) The loop is located near the disk center. In this case, the viewing angle θ (relative to the magnetic field) varies in a wide range along the loop; it is close to zero (or 180°) in the footpoints and equal to 90° at some point near the loop top (see Figure 2). The coordinate s in Figure 2 is the visible distance along the loop axis, *i.e.*, it takes into account the projection effects.
b) The loop is located near the solar limb, and its plane is almost parallel to the equatorial plane (Limb A orientation). In contrast to the previous case, here the viewing angle is close to 90° in the loop footpoints and becomes very small near the loop top.
c) The loop is located near the solar limb, and its plane is almost perpendicular to the line of sight (Limb B orientation). In this case, the viewing angle is always close to 90° and weakly varies along the loop (although it is not constant, which makes this model different from those studied in the work of Reznikova, Antolin, and Van Doorsselaere (2014)).

2.3. Electron Parameters

We assumed that the gyrosynchrotron radio emission is produced by the energetic electrons with the power-law distribution over energy, $f(E) \propto E^{-\delta}$; in the calculations, the energy range is taken to be 100 keV $< E <$ 10 MeV which is typical for the solar flares. The electrons with lower energies are also present in flares, but their contribution to the gyrosynchrotron emission is minor (mostly in the form of self-absorption at low frequencies; see, *e.g.*, Holman 2003) and can usually be ignored. The pitch-angle distribution of the electrons is assumed to be isotropic (*i.e.*, we assumed that it is not affected significantly by the MHD waves). Reznikova, Antolin, and Van Doorsselaere (2014) have considered the case when the concentration of the energetic electrons $n_{\rm b}$ inside the cylinder is proportional to the thermal plasma density, $n_{\rm b\ in}/n_{0\ \rm in} = \text{const}$. Alternatively, one may consider the model in which the energetic electrons are frozen into the magnetic field, so that their concentration is proportional to the field strength, $n_{\rm b\ in}/B_{\rm in} = \text{const}$. However, since in the sausage waves the dominant longitudinal component of the magnetic field B_z and the plasma density n_0 oscillate in phase, both approaches provide almost identical results. In the calculations below we therefore assume that the concentration of the energetic electrons in the loop is always proportional to the thermal plasma density and $n_{\rm b\ in}/n_{0\ \rm in} = 0.025$; in particular, in the equilibrium state we have $n_{\rm b\ in} = 10^8$ and 2.5×10^8 cm^{-3} for the low- and high-density models, respectively. We assume that there are no energetic electrons outside the loop ($n_{\rm b\ out} = 0$).

The gyrosynchrotron radio emission was calculated using the Fast Gyrosynchrotron Codes (Fleishman and Kuznetsov, 2010; Kuznetsov, Nita, and Fleishman, 2011; Nita *et al.*, 2015); these codes include the contribution of the thermal free-free emission as well. We neglected the possible harmonic structure of the gyrosynchrotron emission at low frequencies by using the continuous regime of the fast gyrosynchrotron codes, because in real observations this structure is expected to usually be smoothed by the source inhomogeneity (Kuznetsov, Nita, and Fleishman, 2011); using the continuous approximation also speeds up the calculations appreciably. The codes calculate the emission characteristics by numerically integrating the radiative transfer equations for the ordinary and extraordinary electromag-

netic modes while taking into account the possible mode-coupling effects, *i.e.*, interaction between the modes in the regions of transverse magnetic field (Cohen, 1960; Zheleznyakov and Zlotnik, 1964). This approach is sufficient to accurately reproduce the emission intensity in the quasi-longitudinal and quasi-transverse (with respect to the magnetic field) propagation regimes as well as the circular polarization in the quasi-longitudinal regime (Nita *et al.*, 2015), although simulating the polarization in the regions with $\theta \simeq 90^\circ$ may require considering the full set of Stokes parameters (see the article of Reznikova, Van Doorsselaere, and Kuznetsov (2015)). Only the emission and absorption processes inside the curved magnetic loop are considered, *i.e.*, the emission outside the loop is assumed to propagate like in vacuum.

3. Results

3.1. Equilibrium State

Firstly, we present a brief overview of the emission produced by the loop in the equilibrium state (*i.e.*, without MHD oscillations). This emission is very similar to the emission from an oscillating loop averaged over the wave period. Figure 3 demonstrates the total (spatially integrated) intensity spectra for the loop located at the limb (Limb B orientation). For other orientations, the intensity is slightly lower, but the spectral shapes are qualitatively the same. The concentration of the energetic electrons was chosen such that the spectral maximum (for the low-density model and the spectral index of the energetic electrons of $\delta = 4$) is located at about 10 GHz – a typical value for the continuum microwave emission of solar flares.

The bottom row in Figure 2 demonstrates the simulated distributions of the gyrosynchrotron radio intensity in the equilibrium state along the loop (for the low-density model). The intensity distributions depend on the emission frequency and loop orientation: for the loop located near the disk center, the optically thin emission (*e.g.*, at $\approx$25 GHz) is sharply peaked near the loop top; the same effect is seen for the emission near the spectral peak (at $\approx$10 GHz), while the optically thick emission (*e.g.*, at $\approx$4 GHz) is weakly peaked at the loop footpoints. For the Limb A orientation, the situation is opposite: now the optically thick emission is peaked near the loop top, while the optically thick emission and the emission near the spectral peak are peaked at the loop footpoints. A similar pattern, although with weaker variations, can be seen in the Limb B case. In all cases, there are small narrow

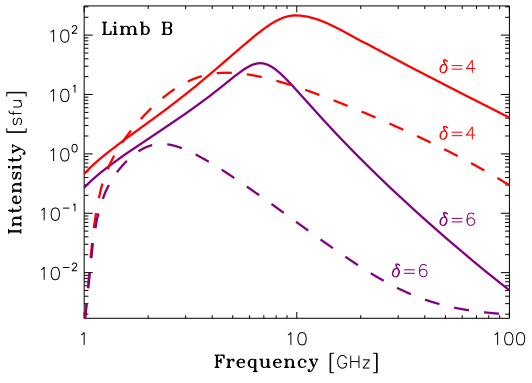

Figure 3 Total (spatially integrated) radio spectra in the equilibrium state. Solid lines: low-density model; dashed lines: high-density model. Two electron spectral indices ($\delta = 4$ and 6) and the Limb B orientation are considered.

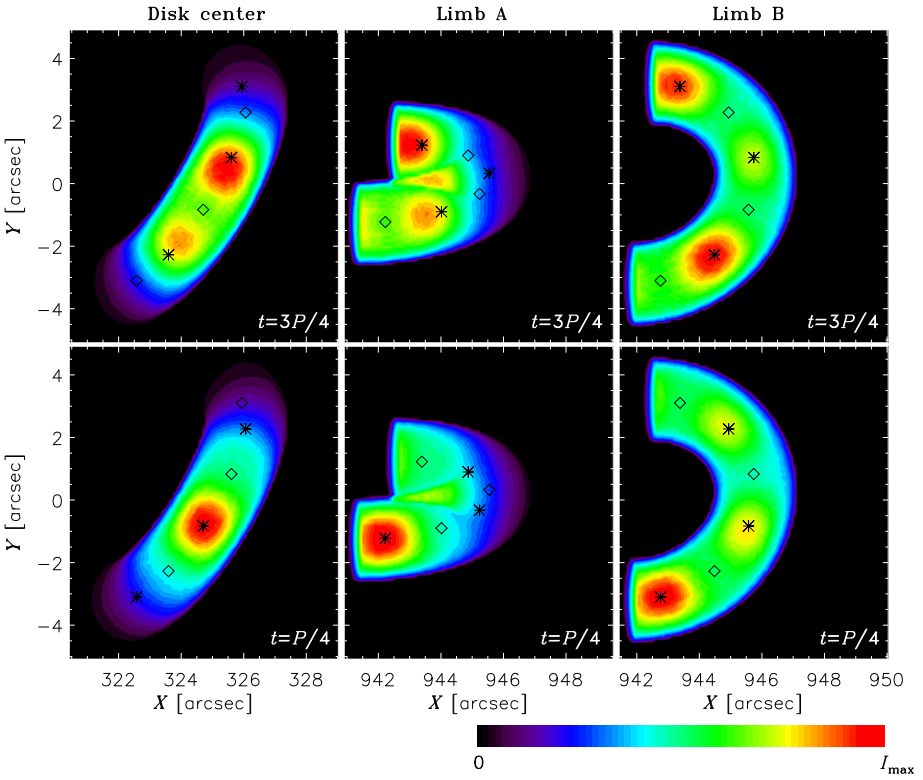

Figure 4 Two-dimensional images of the microwave emission (at a frequency of 25 GHz) for the standing wave. The low-density model is used, the loop contains three sausage waves, and the electron spectral index is $\delta = 4$. Two oscillation phases corresponding to the strongest deviations from the equilibrium are shown. The asterisks ($*$) and diamonds ($\diamond$) mark the points with the strongest/weakest magnetic field at the loop axis.

peaks/dips at the points where the local viewing angle equals 90°; they are caused by different polarization characteristics of the ordinary and extraordinary electromagnetic modes and are typical of the gyrosynchrotron radiation.

3.2. Intensity Modulation: 2D Images

Oscillation-induced variations of the radio emission in different parts of the magnetic loop tend to compensate each other, thus reducing the variations of the total (spatially unresolved) emission. As a result of the varying viewing angle (and hence of the varying local emission parameters) along the loop, this compensation is not complete. Nevertheless, the variations of the total intensity are always much weaker than those of the local (spatially resolved) emission; the amplitude of the total intensity variations decreases with a decrease of the relative wavelength of the MHD waves (*i.e.*, with an increase of the number of the waves in the loop). Therefore we focus below on the characteristics of the spatially resolved emission.

Figure 4 demonstrates the simulated radio images at a frequency of 25 GHz (optically thin emission) for the standing wave. Two opposite oscillation phases are shown. To highlight the effect of the MHD waves, the intensity variations were enhanced as

$$I \to \langle I \rangle + 5\big(I - \langle I \rangle\big), \tag{2}$$

where $\langle I \rangle$ is the intensity averaged over the wave period P:

$$\langle I \rangle = \frac{1}{P} \int_0^P I(t)\,\mathrm{d}t. \tag{3}$$

For the Limb B orientation (with an almost constant viewing angle) the visible emission structure, in general, reflects the structure of the MHD wave: there are three intensity maxima corresponding to the points of the strongest magnetic field (and hence the highest concentration of energetic electrons). For other orientations, the intensity maxima/minima slightly deviate from the magnetic field maxima/minima because of projection effects; furthermore, not all MHD waves are visible (*i.e.*, both the intensity and the oscillation-induced variation amplitude depend strongly on the coordinate along the loop). For the propagating MHD waves, the radio images are similar to those shown in Figure 4, but the brighter/darker spots gradually drift along the loop with time.

3.3. Phase Relations and Modulation Depth

We are interested primarily in the qualitative effects that could reveal the basic MHD wave characteristics (such as the wave mode). As mentioned above, in real flaring loops the MHD wave properties (including the phase speed) can vary strongly along the loop, which is not considered in our model. Therefore it makes no sense to compare, *e.g.*, the simulated time profiles of the emission at the loop top and the footpoints. Instead we consider the local emission parameters, *i.e.*, the temporal delays (phase differences) between the emissions at different frequencies at a given point.

Figures 5 – 6 show the time–distance plots of the normalized intensity variation $(I - \langle I \rangle)/\langle I \rangle$ at the axis of the magnetic loop (*i.e.*, along the line formed by the projection of the loop axis on the image plane) for the low-density model. Four frequencies are shown, representing the optically thick case (4 GHz), a moderately optically thick case (6.3 GHz), the spectral peak (10 GHz), and the optically thin case (25 GHz). Above each panel, the respective maximum modulation depth Δ is given; this value is defined as

$$\Delta = \max \left| \frac{I - \langle I \rangle}{\langle I \rangle} \right|. \tag{4}$$

Note that the maximum modulation depth Δ is different from the average modulation depth ϵ given by Equation (5) (which is used in Section 3.4.2). According to Figures 5 – 6, the maximum modulation depth Δ varies from $\lesssim 1$ % at low frequencies to $\gtrsim 5$ % at high frequencies. These values are relatively low and, in fact, it would be difficult to detect such oscillations in real observations. However, this is because we consider the relatively low-amplitude MHD waves: the variations of the emission source parameters $\delta B/\langle B \rangle$ and $\delta n_\mathrm{b}/\langle n_\mathrm{b} \rangle$ do not exceed 2.5 % and thus the variations of the intensity are comparable to the MHD wave amplitude. The quasi-periodic pulsations reported by Nakariakov, Melnikov, and Reznikova (2003), Melnikov *et al.* (2005), and Reznikova *et al.* (2007) (with the modulation depths of up to ≈ 0.3) require much more powerful MHD waves; nevertheless, if these pulsations are caused by sausage MHD waves, their characteristics should be qualitatively similar to the case studied in this work. Note also that the intensity variations are more pronounced in the optically thin frequency range, in agreement with the results of Mossessian and Fleishman (2012) and Reznikova, Antolin, and Van Doorsselaere (2014).

Figure 5 demonstrates the simulation results for the standing wave. The relative modulation depth, in general (excluding the regions with $\theta \simeq 90°$), follows the same trends as

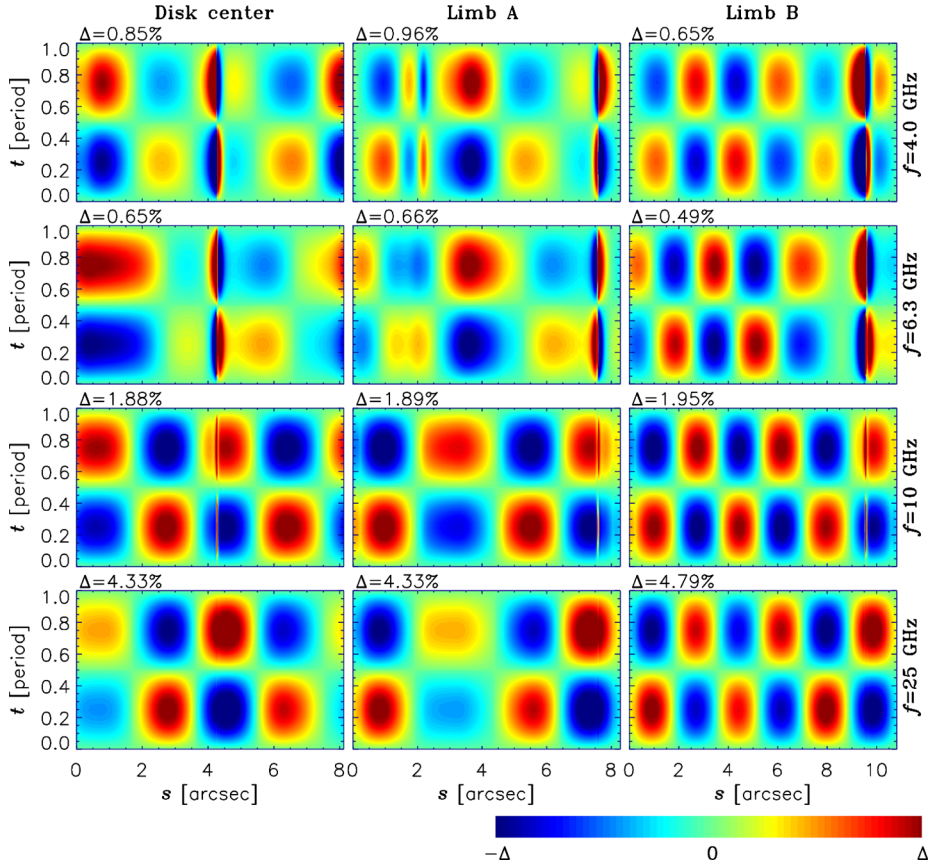

Figure 5 Time–distance plots of the intensity variation: the normalized intensity variation $(I - \langle I \rangle)/\langle I \rangle$ at the loop axis *vs.* the visible coordinate along the loop axis and the oscillation phase. The low-density model (standing wave) is used; the loop contains three sausage waves, and the electron spectral index is $\delta = 4$. For each emission frequency and loop orientation, the maximum modulation depth Δ is given above the corresponding panel.

the unperturbed intensity (see Figure 2): for the loop near the disk center, the modulation depth increases toward the loop top for the optically thin emission ($\gtrsim 10$ GHz) and increases toward the loop footpoints for the optically thick emission (< 10 GHz); for the loops near the limb, the trends are opposite. Oscillations at low ($\lesssim 4$ GHz, the first row of the figure) and high ($\gtrsim 10$ GHz, third and fourth rows) frequencies are synchronous. The fact that the optically thin and thick emissions oscillate in phase agrees with the results of Reznikova, Antolin, and Van Doorsselaere (2014), but contradicts the conclusions of Mossessian and Fleishman (2012). The reason is that in contrast to Mossessian and Fleishman (2012), we take into account the modulation of the viewing angle by the sausage wave, but neglect the modulation of the energy of the nonthermal electrons. In addition, we use the spatially inhomogeneous model in which the source parameters vary along the line of sight; this is especially important for the optically thick emission. Since two different approaches (ours and that of Mossessian and Fleishman (2012)) provide opposite results, we conclude that the sausage-mode MHD waves (at least, in its application to the radio intensity modulation) cannot be treated without a spatially resolved 3D model. Note that this behavior (in-phase

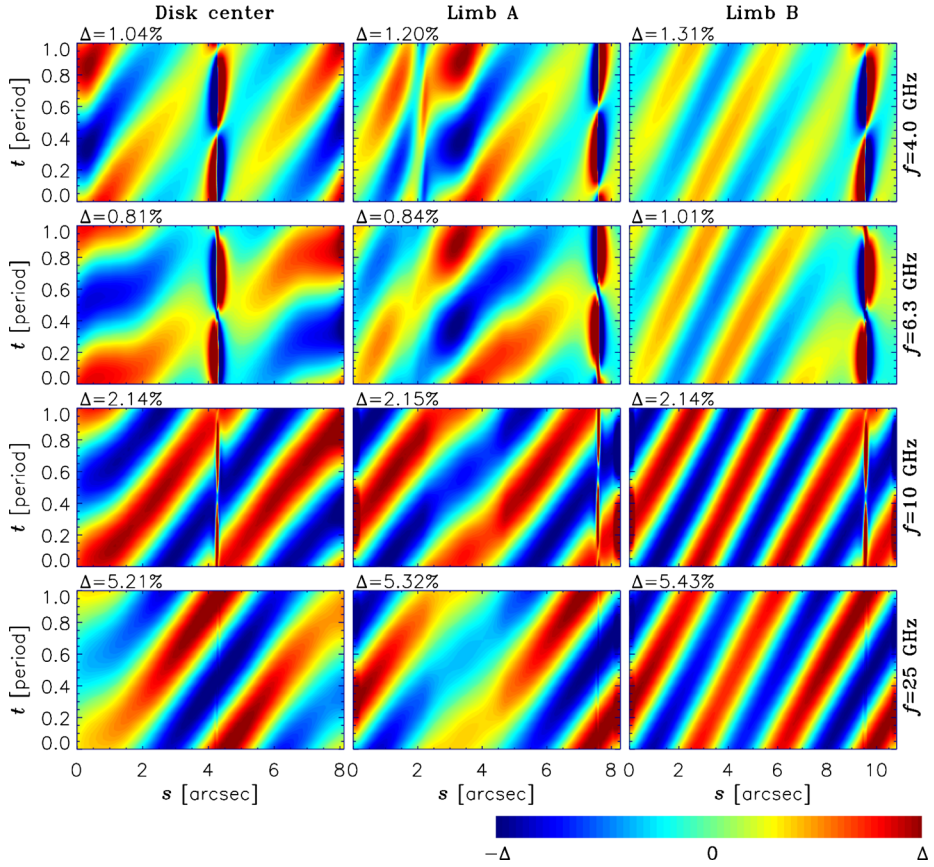

Figure 6 Same as in Figure 5, for the propagating wave.

variations of the optically thin and thick emissions) is observed for all loop orientations and at all locations along the loop; *i.e.*, it is independent of the viewing angle (except for the $\theta = 90^\circ$ case, which is discussed below).

An interesting feature is observed at intermediate frequencies ($\approx$6 GHz, the second row of Figure 5), *i.e.*, in the optically thick range, but not far from the spectral peak; the optical depth τ here exceeds unity, but is not very large ($\tau \approx 10$). The intensity oscillations at these frequencies are shifted by about 1/4 wavelength with respect to the oscillations at higher and lower frequencies. This is caused by the wave-induced variations of the viewing angle: at the intermediate frequencies, these variations (albeit very small) become the main factor modulating the intensity. In contrast, at higher or lower frequencies (with $\tau < 1$ or $\tau \gg 1$), the effect of changing the magnetic field and electron concentration dominates. At the same time, the modulation depth at the intermediate frequencies reaches its minimum (in comparison with other frequency ranges).

The oscillating magnetic field direction (and hence the oscillating viewing angle) also produces some peculiarities in the parts of the loop where the viewing angle is close to 90°. Changing the sign of the magnetic field projection on the line of sight results in changing the dominating electromagnetic wave mode, which affects the intensity. As a result, in the optically thick frequency range the MHD wave induces intensity variations of opposite signs

at different sides of the $\theta = 90^\circ$ stripe; the modulation depth increases sharply. In the optically thin frequency range the intensity variations at different sides of the $\theta = 90^\circ$ stripe have the same sign, and the modulation depth demonstrates only minor variations. It should be noted, however, that these peculiarities only occur in very narrow stripes, which means that detecting them in real observations requires very high spatial resolution.

Similar peculiarities (although without significant changes of the modulation depth) can be seen for the Limb A orientation in the optically thick frequency range at the distance of about $s \simeq 2''$ from the upper footpoint. They occur as a result of the specific loop topology: the optically thick emission is produced near the loop boundary, and for the Limb A orientation (see Figure 2), the dependence of the viewing angle at the loop boundary surface on the coordinate s can become discontinuous; for other loop orientations, this effect is not observed.

Figure 6 demonstrates the simulation results for the propagating wave. Since the structure of the standing and propagating sausage waves is the same, all the above conclusions about the radio intensity oscillations remain valid; the maximum modulation depths shown in Figure 6 are slightly larger than in Figure 5. Using Figure 6, we can track the propagation of the MHD waves and estimate their speed. For the low-density model considered here (see Table 1), the phase speed of the sausage waves equals 8070 km s^{-1}; the visible propagation speed of the radio brightenings/darkenings for the Limb B orientation is very close to this value. However, because of the varying viewing angle, the projected (visible) wave speed varies along the loop; this effect is especially important for the Disk center and Limb A orientations. The amplitude of the propagating radio intensity variations also varies along the loop, with the most notable effects occurring near the regions of transverse (with respect to the line of sight) magnetic field: in these regions, the bright/dark stripes in Figure 6 become discontinuous, although the MHD wave itself has no peculiarities; the bright/dark stripes in the time–distance plots (in the optically thick frequency range) can also become discontinuous in the regions where the viewing angle at the loop boundary sharply depends on the coordinates in the image plane. Thus when interpreting the radio observations with quasi-periodic pulsations, special attention should be paid to the $\theta = 90^\circ$ layers and/or the regions where the visible loop boundary demonstrates topological peculiarities, since they can introduce additional phase shifts that do not reflect the properties of the underlying MHD waves.

Assuming that the relative intensity variations are approximately proportional to the relative MHD wave amplitude, we can estimate that the MHD waves with the amplitude $\delta B/\langle B\rangle$ of about 40 – 50 % (with other source parameters the same as in Figures 5 – 6) should produce an intensity modulation depth of up to 100 %. However, simulating the MHD waves with such amplitudes requires taking into account nonlinear effects. As we show in Sections 3.4.2 – 3.4.3, the emission modulation depth increases for softer electron beams or for higher plasma densities at low frequencies (when the Razin effect is important), although this increase of the modulation depth is always accompanied by a sharp decrease of the intensity.

3.4. Parametric Study

We now consider how the fluctuations of the radio emission depend on various parameters of the flaring loop.

3.4.1. Effect of the Wave Number

Figure 7 demonstrates the time–distance plots of the intensity variation for the models with increased numbers of MHD waves in the magnetic loop (four and six waves, which corresponds to loop lengths of 11 300 and 16 950 km, respectively); the simulation results shown

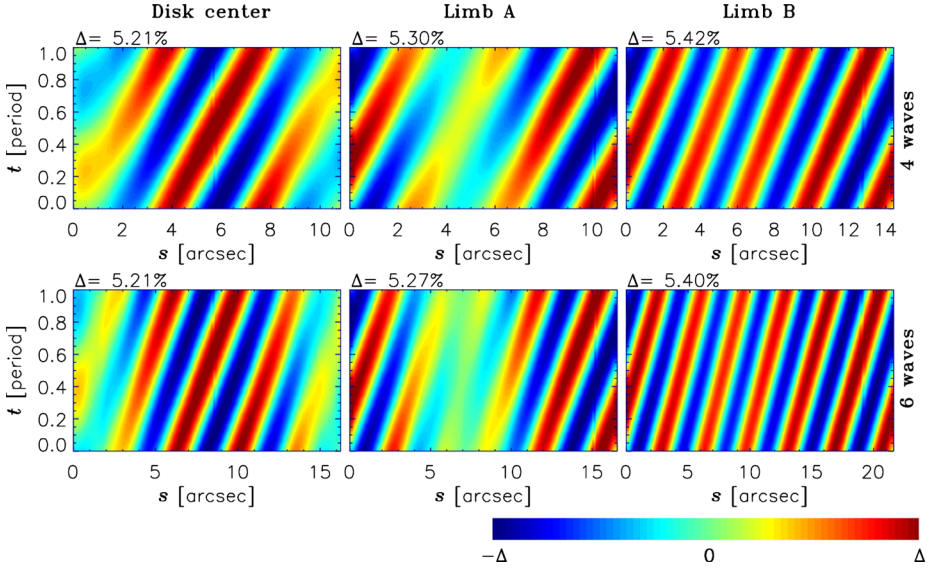

Figure 7 Time–distance plots of the intensity variation at the loop axis (same as in Figures 5 – 6) at the frequency of 25 GHz for different loop orientations and different numbers of wavelengths (four and six) in the loop. The low-density model (propagating wave) is used, and the electron spectral index is $\delta = 4$.

correspond to the low-density model, a nonthermal electron spectral index of $\delta = 4$, and the optically thin emission (at a frequency of 25 GHz). As we showed above, the standing and propagating MHD waves affect the radio emission in a qualitatively similar way; therefore only the results for the propagating wave are shown.

Our simulations have revealed no significant effect of the number of the MHD waves in the loop, *i.e.*, both the emission modulation depth and the phase relations between the emissions at different frequencies remain the same. The only difference can be noticed in the regions where the loop axis becomes nearly parallel to the line of sight, *i.e.*, near the loop footpoints for the Disk center orientation and near the loop top for the Limb A orientation: since the length of the formation region of the optically thin emission can exceed an MHD wavelength, the effects of variation of the magnetic field and electron concentration in different parts of the emission source (with opposite phases) can compensate each other. As a result, the amplitude of the intensity oscillations decreases with a decrease of the relative (with respect to the loop length) MHD wavelength. This effect is not observed in the optically thick frequency range.

It can be seen in Figure 7 (as well as in Figures 4 – 6) that the MHD observations are best resolved when the magnetic tube is observed in a nearly perpendicular direction. Indeed, for the Limb B orientation there is a one-to-one correspondence between the MHD waves and the spatial and temporal structure of the radio emission. For other orientations, this correspondence is less straightforward, and some MHD wave nodes can even be missing in the radio emission; as expected, the radio emission cannot accurately reflect the MHD wave structure in the regions where the viewing angle with respect to the magnetic field θ is small. While it is challenging to estimate the number of observed MHD wave nodes in a general case, we expect (and this is confirmed by the simulations) that the MHD wave nodes are absent from the radio emission in the regions with $\tan\theta \lesssim R/\lambda$, where R is the loop radius and λ is the MHD wavelength; this is caused either by the averaging along the line of sight

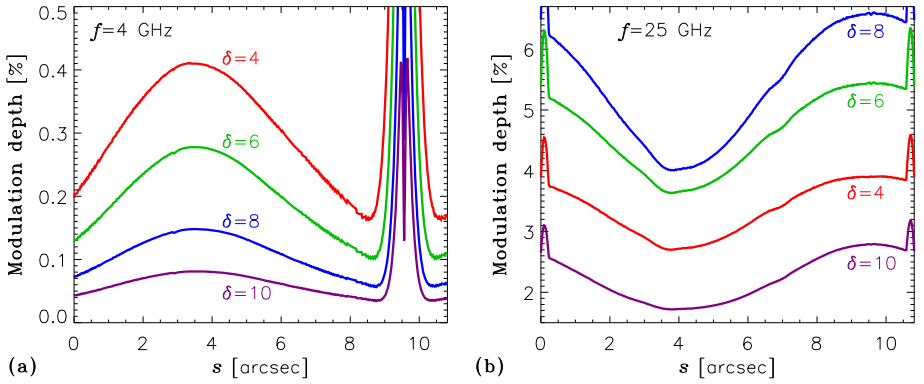

Figure 8 Average modulation depth of the intensity at the loop axis for different frequencies and different spectral indices of the energetic electrons. The low-density model (propagating wave) and the Limb B orientation are considered.

(in the optically thin frequency range) or by the strong reabsorption of the emission during propagation (in the optically thick frequency range). Note also that, as we discussed above, the $\theta = 90^\circ$ layers can introduce the patterns in the radio emission (at low frequencies) similar to additional MHD waves.

3.4.2. Effect of the Spectral Index of Energetic Electrons

The energy spectrum of the radio-emitting electrons greatly affects the gyrosynchrotron emission. As can be seen from Figure 3, softer electron beams (with larger spectral indices δ) produce less intense emission with steeper spectrum slope in the optically thin frequency range; the spectral peak shifts to lower frequencies. We found that the variation of the spectral index δ does not qualitatively change the simulated radio images (like in Figure 4). However, there are quantitative changes in the emission time profiles that may affect detectability of the MHD oscillations.

Figure 8 demonstrates the average modulation depths of the intensity (for the propagating MHD wave, three sausage waves per loop, low-density model, and Limb B orientation); the emission at the loop axis is considered and the values are plotted as functions of the coordinate along the loop. The average modulation depth ϵ is calculated as (Mossessian and Fleishman, 2012)

$$\epsilon = \frac{m}{\langle I \rangle}, \qquad m^2 = \frac{1}{P}\int_0^P \left[I(t) - \langle I \rangle\right]^2 \mathrm{d}t; \tag{5}$$

it is related to the maximum modulation depth Δ (shown in Figures 5 – 7) as $\Delta \simeq \epsilon\sqrt{2}$. In the optically thin frequency range (Figure 8b) an increase in the spectral index results firstly in an increase in the modulation depth. As a result, the oscillation-modulated radio images become more contrasted and the periodic variations of the emission become easier to detect. For even higher electron spectral indices ($\delta \gtrsim 10$ for the considered frequency of 25 GHz), the modulation depth decreases sharply because the gyrosynchrotron emission becomes too weak and the emission is produced mainly by the free-free mechanism that is weakly affected by the MHD oscillations. In the optically thick frequency range (Figure 8a) the modulation depths are small ($\lesssim 0.5$ %) and decrease with increasing δ.

As mentioned above, Figure 8 corresponds to the propagating wave and Limb B orientation; for other orientations and/or for the standing wave, these conclusions remain valid. Assuming that the relative intensity variations are approximately proportional to the relative MHD wave amplitude, we can estimate that for the electron spectral index of $\delta = 8$ and the MHD wave amplitude $\delta B/\langle B\rangle$ of about 25 – 30 %, the average (ϵ) and maximum (Δ) modulation depths in the optically thin frequency range should reach ≈ 70 % and ≈ 100 %, respectively; the MHD waves with such amplitudes seem to be feasible.

3.4.3. Effect of the Plasma Density

Finally, we consider the case when the spectral peak of the gyrosynchrotron radio emission is formed by the Razin effect (Razin, 1960a,b). This effect takes place in a relatively high-density plasma and results in a considerable suppression of the gyrosynchrotron emission at the frequencies below

$$f_{\mathrm{R}} \simeq \frac{2}{3}\frac{f_{\mathrm{p}}^2}{f_{\mathrm{B}}}, \tag{6}$$

where f_{p} and f_{B} are the plasma and cyclotron frequencies in the emission source, respectively. At frequencies below f_{R}, the variations of the thermal plasma density should become the main factor affecting the radio intensity.

As an illustrative example, we use the high-density model (see Table 1). As can be seen from Figure 3, in this case the Razin frequency f_{R} is about 4 GHz. Thus at the frequencies well above 4 GHz the intensity variations should be caused mainly by the oscillations of the magnetic field and energetic electron concentration (like in the low-density model), at the frequencies below 4 GHz the intensity variations should be caused mainly by the Razin effect (*i.e.*, by the oscillating plasma density), while at the frequencies around the spectral peak (≈ 4 GHz) both factors should be important.

Figure 9 demonstrates the simulation results (time–distance plots of the intensity variation) at three different frequencies for the high-density model, standing sausage wave, and the nonthermal electrons spectral index of $\delta = 4$. In the optically thin frequency range, the modulation depth of the intensity is larger than that for the low-density model because of the model parameters used (the relative MHD wave amplitude for the high-density model is larger, see Table 1). The modulation depth reaches its minimum at a frequency below the spectral peak (≈ 2 GHz, depending on the viewing angle) and then rapidly increases with decreasing frequency; however, as can be seen in Figure 3, the intensity at these frequencies also becomes very low, so that detecting the intensity oscillations in observations would be difficult.

It can be seen in Figure 9 that for the Limb B orientation (when the viewing angle is close to 90°) the radio oscillations in the optically thin frequency range ($\gtrsim 10$ GHz) and near the spectral peak (≈ 4 GHz) are synchronous (in phase), while the low-frequency emission ($\lesssim 2$ GHz) oscillates in anti-phase with the emissions at higher frequencies; the phase reversal occurs (for $\theta \simeq 90°$) at ≈ 2 GHz. Clearly, this result indicates that at high frequencies (above and even slightly below the spectral peak) the intensity variations are caused by the variations of the magnetic field and nonthermal electrons concentration, while at lower frequencies (< 2 GHz) the Razin effect dominates; these factors affect the emission in opposite ways.

A similar picture can be seen for two other loop orientations in the regions where the viewing angle is close to 90° (*i.e.*, near the loop top for the Disk center orientation and near the footpoints for the Limb A orientation). For smaller viewing angles the picture is more

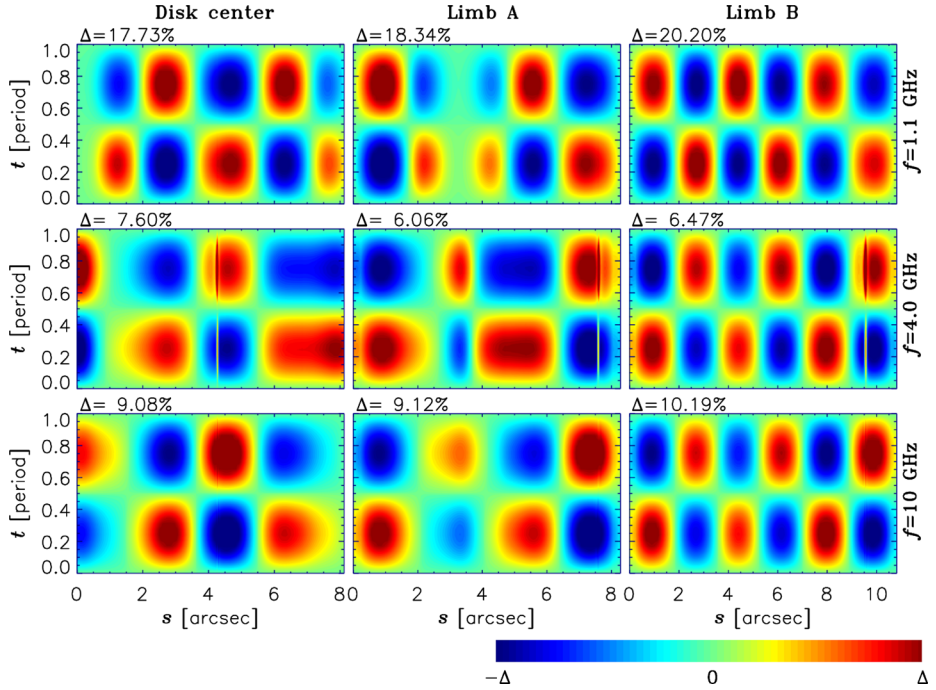

Figure 9 Time–distance plots of the intensity variation at the loop axis (same as in Figures 5 – 7) for the high-density model. A standing wave is considered, and the electron spectral index is $\delta = 4$.

complicated, since both the modulation depth and the above-mentioned frequency of the oscillation phase reversal are angle-dependent: the frequency of the phase reversal increases with a decrease of the viewing angle. As a result, if the viewing angle varies gradually along the loop, we can see either correlation or anticorrelation between the oscillations at two given frequencies, depending on the coordinate s.

These results contradict the conclusions of Mossessian and Fleishman (2012), who have found that the oscillations of the high- and low-frequency emissions (in the case when the Razin effect is important) should occur strictly in phase. As mentioned before (see Section 3.3), this is because we considered a slightly different model for the variation of the parameters in the sausage wave as well as a spatially inhomogeneous emission source. Our results also disagree with the conclusions of Reznikova, Antolin, and Van Doorsselaere (2014), who have found that the oscillations of the high- and low-frequency emissions occur mostly in phase (although this conclusion was dependent on the viewing angle). Most likely, this is because Reznikova, Antolin, and Van Doorsselaere (2014) considered the emission with the frequencies below the spectral peak but above the "phase reversal frequency" so that the effect of the Razin suppression was too weak.

4. Conclusions

We have simulated the modulation of the gyrosynchrotron radio emission by the sausage-mode MHD oscillations in a semi-circular magnetic loop in an application to the solar flares.

Although the model does not include the variation of the magnetic field and plasma parameters with height, it has allowed us to study the effect of varying the viewing angle along the loop. We considered three loop orientations and different parameters of the magnetic field, plasma, and energetic particles. In particular, we studied in detail the phase relations between the spatially resolved intensity oscillations at different frequencies. The results are summarized as follows:

- In the model with a relatively low plasma density (when the Razin effect is negligible), the high-frequency (optically thin) and low-frequency (optically thick) emissions oscillate, as a rule, in phase. An exception is the optically thick emission at the frequencies just below the spectral peak, whose oscillations are shifted by $\approx 1/4$ MHD wavelength with respect to the oscillations at other frequencies.
- In the model with a relatively high plasma density (when the Razin effect is important), the emissions at high and low frequencies oscillate in anti-phase. The reversal of the oscillation phase occurs, as a rule, at a frequency well below the spectral peak; this frequency depends on the viewing angle.
- In the optically thin frequency range, both the unperturbed intensity and the absolute and relative intensity variations are largest in the regions where the local magnetic field is nearly perpendicular to the line of sight. In contrast, in the optically thick frequency range all the mentioned values are the largest in the regions with small viewing angles.
- In the optically thin frequency range, the intensity oscillations are more pronounced for softer electron beams (*i.e.*, with higher spectral indices). The trend is opposite in the optically thick frequency range.
- In the optically thick frequency range, the intensity oscillations can have sharp phase shifts between the adjacent regions due to the presence of layers of a transverse (with respect to the line of sight) magnetic field and other topological peculiarities.
- Averaging over the visible source area and/or along the line of sight reduces the amplitude of the intensity oscillations; this effect becomes more important with an increase in the number of the MHD harmonics in the loop.

This last result means that for a limited spatial resolution, the real observations can differ from the ideal simulations presented here. Nevertheless, we expect that if an instrument spatial resolution is better than a MHD wavelength, this will allow us to detect (or rule out) the above-mentioned phase relations between the oscillations at different frequencies; another requirement is the ability to perform imaging observations at many frequencies. We anticipate that the forthcoming multiwavelength radioheliographs (such as the Expanded Owens Valley Solar Array, Upgraded Siberian Solar Radio Telescope, and Chinese Spectral Radioheliograph; see the review of Nakariakov, Kashapova, and Yan (2014) and references therein) will be able to provide the necessary data.

Acknowledgements This work was supported in part by the Russian Foundation of Basic Research (grants 12-02-00173, 13-02-90472 and 14-02-91157) and by a Marie Curie International Research Staff Exchange Scheme "Radiosun" (PEOPLE-2011-IRSES-295272). The research leading to the presented results has been sponsored by an Odysseus grant of the FWO Vlaanderen. It has been performed in the context of the IAP P7/08 CHARM (Belspo) and the GOA-2015-014 (KU Leuven).

Appendix: Toroidal Coordinates

As was mentioned above, we consider the MHD waves in an overdense cylinder; the system can be described by the cylindrical coordinates: the distance along the cylinder axis z, the

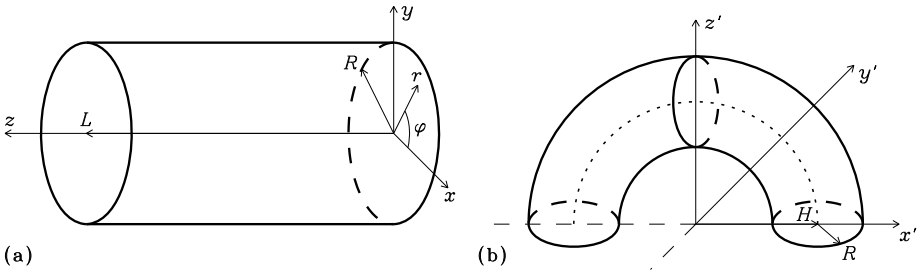

Figure 10 (a) Sketch of the model plasma cylinder. (b) Sketch of the model semi-toroidal loop.

distance from this axis r, and the azimuthal angle φ (see Figure 10a). We assume that the cylinder has the length L (*i.e.*, $0 \le z \le L$) and the radius R (the radio emission is produced only inside the cylinder, *i.e.*, at $r \le R$).

The cylinder is assumed to be bent into a semi-circular (semi-toroidal) loop (see Figure 10b); the loop curvature radius is $H = L/\pi$ (evidently, we need $H > R$). We assume that initially the loop is oriented as shown in Figure 10b, *i.e.*, it is vertical, symmetric with respect to the $x'z'$ and $y'z'$ planes, and its axial line lies in the $x'z'$ plane. Then the cylindrical coordinates (z, r, φ) are related to the Cartesian coordinates (x', y', z') as

$$x' = (r\cos\varphi + H)\cos\chi, \tag{7}$$

$$y' = r\sin\varphi, \tag{8}$$

$$z' = (r\cos\varphi + H)\sin\chi, \tag{9}$$

and

$$\tan\chi = \frac{z'}{x'}, \tag{10}$$

$$r^2 = \left(x' - H\cos\chi\right)^2 + \left(y'\right)^2 + \left(z' - H\sin\chi\right)^2, \tag{11}$$

$$\tan\varphi = \frac{y'}{x'\cos\chi + z'\sin\chi - H}, \tag{12}$$

where $\chi = z/L$.

Assume that a vector $\mathbf{A}$ at a given point is defined by its three components (A_z, A_r, A_φ) in the cylindrical coordinate system. After transformation to the semi-circular loop, the vector can be expressed as $\mathbf{A}' = A_z\mathbf{a}'_z + A_r\mathbf{a}'_r + A_\varphi\mathbf{a}'_\varphi$, where the unit vectors $\mathbf{a}'_{z,r,\varphi}$ in the Cartesian coordinates are given by

$$\mathbf{a}'_z = (-\sin\chi, 0, \cos\chi), \tag{13}$$

$$\mathbf{a}'_r = (\cos\varphi\cos\chi, \sin\varphi, \cos\varphi\sin\chi), \tag{14}$$

$$\mathbf{a}'_\varphi = (-\sin\varphi\cos\chi, \cos\varphi, -\sin\varphi\sin\chi). \tag{15}$$

These formulae are valid in a general case. We here considered the azimuthally symmetric case when all parameters are independent of the azimuthal angle φ and the azimuthal components A_φ of all vectors are equal to zero.

The orientation shown in Figure 10b corresponds to the vertical loop located at the center of the solar disk, with the axis z' being the line of sight and the plane $x'z'$ being the equatorial

plane. All other orientations (see, *e.g.*, Figure 2) are obtained by rotating the loop firstly by the angle ψ around the local vertical (z' axis) and then by the angle λ around the solar rotation axis.

References

Alissandrakis, C.E., Preka-Papadema, P.: 1984, Microwave emission and polarization of a flaring loop. *Astron. Astrophys.* **139**, 507.

Altyntsev, A.T., Fleishman, G.D., Huang, G.L., Melnikov, V.F.: 2008, A broadband microwave burst produced by electron beams. *Astrophys. J.* **677**, 1367. DOI.

Andries, J., Cally, P.S.: 2011, On the dispersion and scattering of magnetohydrodynamic waves by longitudinally stratified flux tubes. *Astrophys. J.* **743**, 164. DOI.

Andries, J., Goossens, M., Hollweg, J.V., Arregui, I., Van Doorsselaere, T.: 2005, Coronal loop oscillations. Calculation of resonantly damped MHD quasi-mode kink oscillations of longitudinally stratified loops. *Astron. Astrophys.* **430**, 1109. DOI.

Antolin, P., Van Doorsselaere, T.: 2013, Line-of-sight geometrical and instrumental resolution effects on intensity perturbations by sausage modes. *Astron. Astrophys.* **555**, A74. DOI.

Aschwanden, M.J.: 1987, Theory of radio pulsations in coronal loops. *Solar Phys.* **111**, 113. DOI.

Aschwanden, M.J., Fletcher, L., Schrijver, C.J., Alexander, D.: 1999, Coronal loop oscillations observed with the Transition Region and Coronal Explorer. *Astrophys. J.* **520**, 880. DOI.

Bastian, T.S., Benz, A.O., Gary, D.E.: 1998, Radio emission from solar flares. *Annu. Rev. Astron. Astrophys.* **36**, 131. DOI.

Chen, P.F., Priest, E.R.: 2006, Transition-region explosive events: Reconnection modulated by p-mode waves. *Solar Phys.* **238**, 313. DOI.

Cohen, M.H.: 1960, Magnetoionic mode coupling at high frequencies. *Astrophys. J.* **131**, 664. DOI.

Costa, J.E.R., Simões, P.J.A., Pinto, T.S.N., Melnikov, V.F.: 2013, Solar burst analysis with 3D loop models. *Publ. Astron. Soc. Japan* **65**, 5. DOI.

De Moortel, I., Nakariakov, V.M.: 2012, Magnetohydrodynamic waves and coronal seismology: An overview of recent results. *Phil. Trans. Roy. Soc. London Ser. A* **370**, 3193. DOI.

Doyle, J.G., Popescu, M.D., Taroyan, Y.: 2006, Repetitive occurrence of explosive events at a coronal hole boundary. *Astron. Astrophys.* **446**, 327. DOI.

Edwin, P.M., Roberts, B.: 1983, Wave propagation in a magnetic cylinder. *Solar Phys.* **88**, 179. DOI.

Erdélyi, R.: 2006, Magnetic coupling of waves and oscillations in the lower solar atmosphere: Can the tail wag the dog? *Phil. Trans. Roy. Soc. London Ser. A* **364**, 351. DOI.

Fleishman, G.D., Bastian, T.S., Gary, D.E.: 2008, Broadband quasi-periodic radio and X-ray pulsations in a solar flare. *Astrophys. J.* **684**, 1433. DOI.

Fleishman, G.D., Kuznetsov, A.A.: 2010, Fast gyrosynchrotron codes. *Astrophys. J.* **721**, 1127. DOI.

Fleishman, G.D., Melnikov, V.F.: 2003, Gyrosynchrotron emission from anisotropic electron distributions. *Astrophys. J.* **587**, 823. DOI.

Fletcher, L., Hudson, H.S.: 2008, Impulsive phase flare energy transport by large-scale Alfvén waves and the electron acceleration problem. *Astrophys. J.* **675**, 1645. DOI.

Gary, D.E., Fleishman, G.D., Nita, G.M.: 2013, Magnetography of solar flaring loops with microwave imaging spectropolarimetry. *Solar Phys.* **288**, 549. DOI.

Gruber, D., Lachowicz, P., Bissaldi, E., Briggs, M.S., Connaughton, V., Greiner, J., van der Horst, A.J., Kanbach, G., Rau, A., Bhat, P.N., Diehl, R., von Kienlin, A., Kippen, R.M., Meegan, C.A., Paciesas, W.S., Preece, R.D., Wilson-Hodge, C.: 2011, Quasi-periodic pulsations in solar flares: New clues from the Fermi Gamma-Ray Burst Monitor. *Astron. Astrophys.* **533**, A61. DOI.

Holman, G.D.: 2003, The effects of low- and high-energy cutoffs on solar flare microwave and hard X-ray spectra. *Astrophys. J.* **586**, 606. DOI.

Klein, K.L., Trottet, G.: 1984, Gyrosynchrotron radiation from a source with spatially varying field and density. *Astron. Astrophys.* **141**, 67.

Kliem, B., Karlický, M., Benz, A.O.: 2000, Solar flare radio pulsations as a signature of dynamic magnetic reconnection. *Astron. Astrophys.* **360**, 715.

Kopylova, Y.G., Stepanov, A.V., Tsap, Y.T.: 2002, Radial oscillations of coronal loops and microwave radiation from solar flares. *Astron. Lett.* **28**, 783. DOI.

Kucera, T.A., Dulk, G.A., Kiplinger, A.L., Winglee, R.M., Bastian, T.S., Graeter, M.: 1993, Multiple wavelength observations of an off-limb eruptive solar flare. *Astrophys. J.* **412**, 853. DOI.

Kundu, M.R., Nindos, A., White, S.M., Grechnev, V.V.: 2001, A multiwavelength study of three solar flares. *Astrophys. J.* **557**, 880. DOI.

Kupriyanova, E.G., Melnikov, V.F., Nakariakov, V.M., Shibasaki, K.: 2010, Types of microwave quasi-periodic pulsations in single flaring loops. *Solar Phys.* **267**, 329. DOI.
Kuznetsov, A.A., Kontar, E.P.: 2015, Spatially resolved energetic electron properties for the 21 May 2004 flare from radio observations and 3D simulations. *Solar Phys.* **290**, 79. DOI.
Kuznetsov, S.A., Melnikov, V.F.: 2012, Modeling the effect of plasma density on the dynamics of the microwave spectrum of solar flaring loops. *Geomagn. Aeron.* **52**, 883. DOI.
Kuznetsov, A.A., Nita, G.M., Fleishman, G.D.: 2011, Three-dimensional simulations of gyrosynchrotron emission from mildly anisotropic nonuniform electron distributions in symmetric magnetic loops. *Astrophys. J.* **742**, 87. DOI.
Kuznetsov, A.A., Zharkova, V.V.: 2010, Manifestations of energetic electrons with anisotropic distributions in solar flares. II. Gyrosynchrotron microwave emission. *Astrophys. J.* **722**, 1577. DOI.
Melnikov, V.F., Reznikova, V.E., Shibasaki, K., Nakariakov, V.M.: 2005, Spatially resolved microwave pulsations of a flare loop. *Astron. Astrophys.* **439**, 727. DOI.
Melrose, D.B.: 1968, The emission and absorption of waves by charged particles in magnetized plasmas. *Astrophys. Space Sci.* **2**, 171. DOI.
Mossessian, G., Fleishman, G.D.: 2012, Modeling of gyrosynchrotron radio emission pulsations produced by magnetohydrodynamic loop oscillations in solar flares. *Astrophys. J.* **748**, 140. DOI.
Nakariakov, V.M., Kashapova, L.K., Yan, Y.H.: 2014, Editorial: Solar radiophysics – Recent results on observations and theories. *Res. Astron. Astrophys.* **14**, 1. DOI.
Nakariakov, V.M., Melnikov, V.F.: 2006, Modulation of gyrosynchrotron emission in solar and stellar flares by slow magnetoacoustic oscillations. *Astron. Astrophys.* **446**, 1151. DOI.
Nakariakov, V.M., Melnikov, V.F.: 2009, Quasi-periodic pulsations in solar flares. *Space Sci. Rev.* **149**, 119. DOI.
Nakariakov, V.M., Melnikov, V.F., Reznikova, V.E.: 2003, Global sausage modes of coronal loops. *Astron. Astrophys.* **412**, L7. DOI.
Nakariakov, V.M., Verwichte, E.: 2005, Coronal waves and oscillations. *Living Rev. Solar Phys.* **2**(3). DOI. http://solarphysics.livingreviews.org/Articles/lrsp-2005-3/.
Nakariakov, V.M., Ofman, L., Deluca, E.E., Roberts, B., Davila, J.M.: 1999, TRACE observation of damped coronal loop oscillations: Implications for coronal heating. *Science* **285**, 862. DOI.
Nakariakov, V.M., Foullon, C., Verwichte, E., Young, N.P.: 2006, Quasi-periodic modulation of solar and stellar flaring emission by magnetohydrodynamic oscillations in a nearby loop. *Astron. Astrophys.* **452**, 343. DOI.
Nindos, A., White, S.M., Kundu, M.R., Gary, D.E.: 2000, Observations and models of a flaring loop. *Astrophys. J.* **533**, 1053. DOI.
Nita, G.M., Fleishman, G.D., Kuznetsov, A.A., Kontar, E.P., Gary, D.E.: 2015, Three-dimensional radio and X-ray modeling and data analysis software: Revealing flare complexity. *Astrophys. J.* **799**, 236. DOI.
Preka-Papadema, P., Alissandrakis, C.E.: 1988, Spatial and spectral structure of a solar flaring loop at centimeter wavelengths. *Astron. Astrophys.* **191**, 365.
Preka-Papadema, P., Alissandrakis, C.E.: 1992, Two-dimensional model maps of flaring loops at cm-wavelengths. *Astron. Astrophys.* **257**, 307.
Ramaty, R.: 1969, Gyrosynchrotron emission and absorption in a magnetoactive plasma. *Astrophys. J.* **158**, 753. DOI.
Razin, V.A.: 1960a, On the theory of radio spectra of discrete sources at the frequencies below 30 MHz. *Izv. Vysš. Učebn. Zaved. Radiofiz.* **3**, 584.
Razin, V.A.: 1960b, On the spectrum of nonthermal cosmic radio emission. *Izv. Vysš. Učebn. Zaved. Radiofiz.* **3**, 921.
Reznikova, V.E., Antolin, P., Van Doorsselaere, T.: 2014, Forward modeling of gyrosynchrotron intensity perturbations by sausage modes. *Astrophys. J.* **785**, 86. DOI.
Reznikova, V.E., Van Doorsselaere, T., Kuznetsov, A.A.: 2015, Perturbations of gyrosynchrotron emission polarization from solar flares by sausage modes: Forward modeling. *Astron. Astrophys.* **575**, A47. DOI. ADS.
Reznikova, V.E., Melnikov, V.F., Su, Y., Huang, G.: 2007, Pulsations of microwave flaring emission at low and high frequencies. *Astron. Rep.* **51**, 588. DOI.
Reznikova, V.E., Melnikov, V.F., Shibasaki, K., Gorbikov, S.P., Pyatakov, N.P., Myagkova, I.N., Ji, H.: 2009, 2002 August 24 limb flare loop: Dynamics of microwave brightness distribution. *Astrophys. J.* **697**, 735. DOI.
Simões, P.J.A., Costa, J.E.R.: 2006, Solar bursts gyrosynchrotron emission from three-dimensional sources. *Astron. Astrophys.* **453**, 729. DOI.
Simões, P.J.A., Costa, J.E.R.: 2010, Gyrosynchrotron emission from anisotropic pitch-angle distribution of electrons in 3-D solar flare sources. *Solar Phys.* **266**, 109. DOI.

Tzatzakis, V., Nindos, A., Alissandrakis, C.E.: 2008, A statistical study of microwave flare morphologies. *Solar Phys.* **253**, 79. DOI.

Van Doorsselaere, T., Debosscher, A., Andries, J., Poedts, S.: 2004, The effect of curvature on quasi-modes in coronal loops. *Astron. Astrophys.* **424**, 1065. DOI.

Zaitsev, V.V., Stepanov, A.V.: 1975, On the origin of pulsations of type IV solar radio emission. Plasma cylinder oscillations (I). *Issled. Geomagn. Aèron. Fiz. Solnca* **37**, 3.

Zheleznyakov, V.V., Zlotnik, E.Y.: 1964, Polarization of radio waves passing through a transverse magnetic field region in the solar corona. *Soviet Astron.* **7**, 485.